Versatile and automated workflow for the analysis of oligodendroglial calcium signals in preclinical mouse models of myelin repair

Dorien A Maas, Blandine Manot-Saillet, Philippe Bun, Chloé Habermacher,
Corinne Poilbout, Filippo Rusconi, Maria Cecilia Angulo

1   **Versatile and automated workflow for the analysis of oligodendroglial calcium signals in preclinical**

2   **mouse models of myelin repair**

3

4   Dorien A. Maas[1]*, Blandine Manot-Saillet[1]*, Philippe Bun[2], Chloé Habermacher[1,6], Corinne Poilbout,

5   Filippo Rusconi[4,5], Maria Cecilia Angulo[1,3]

6

7   *1 Université Paris Cité, Institute of Psychiatry and Neuroscience of Paris (IPNP), INSERM U1266, "Team: Interactions*

8   *between neurons and oligodendroglia in myelination and myelin repair", F-75014 Paris, France*

9   *2 Université Paris Cité, Institute of Psychiatry and Neuroscience of Paris (IPNP), INSERM U1266, "NeurImag*

10   *platform", F-75014 Paris, France*

11   *3 GHU PARIS psychiatrie & neurosciences, F-75014 Paris, France*

12   *4 IDEEV, GQE, Université Paris-Saclay, CNRS, INRAE, AgroParisTech, 12, route 128, F-91272 Gif-sur-Yvette, France*

13   *5 INSERM, UMR-S 1138, Centre de Recherche des Cordeliers, France; Sorbonne Université-INSERM, France; PAPPSO,*

14   *Universite Paris-Saclay, INRAE, CNRS, France*

15   *6 Present address: SynapCell, Bâtiment Synergy Zac Isiparc, F-38330 Saint Ismier, France*

16   * These authors contributed equally to this work

17

18   **Corresponding author:**

19   María Cecilia Angulo, Institute of Psychiatry and Neuroscience of Paris (IPNP), INSERM 1266, 102, rue de

20   la   Santé,   75014   Paris,   FRANCE.   Tel: 33-1-40789243.   e-mail   address: maria-

21   cecilia.angulo@parisdescartes.fr

Abstract

Intracellular Ca^{2+} signals of oligodendroglia, the myelin-forming cells of the central nervous system, regulate vital cellular processes including myelination. However, studies on oligodendroglia Ca^{2+} signal dynamics are still scarce, especially during myelin repair, and there are no software solutions to properly analyze the unique Ca^{2+} signal characteristics in these cells. Here, we provide a comprehensive experimental and analytical workflow to acquire and analyze Ca^{2+} imaging data of oligodendroglia at the population and single-cell levels in preclinical mouse models of myelin repair. We report diverse *ex vivo* and *in vivo* experimental protocols to obtain reproducible Ca^{2+} imaging data from oligodendroglia in demyelinated lesions. Importantly, we provide an analytical pipeline containing two free, open source and cross-platform software programs, Occam and post-prOccam, that enable the fully automated analysis of one- and two-photon Ca^{2+} imaging datasets from oligodendroglia obtained by either *ex vivo* or *in vivo* Ca^{2+} imaging techniques. This versatile and accessible experimental and analytical framework, which revealed significant but uncorrelated spontaneous Ca^{2+} activity in oligodendroglia inside demyelinated lesions, should facilitate the elucidation of Ca^{2+}-mediated mechanisms underlying remyelination and therefore help to accelerate the development of therapeutic strategies for the many myelin-related disorders, such as multiple sclerosis.

Introduction

In demyelinating diseases such as multiple sclerosis (MS), myelin sheaths produced by oligodendrocytes (OL) are destroyed by the immune system, resulting in OL death and axonal degeneration and, ultimately, in both physical and neurological disabilities (Duncan & Radcliff, 2016). Upon demyelination, new oligodendrocyte precursor cells (OPCs) and OLs can be generated and partial myelin repair can take place (Franklin & Ffrench-Constant, 2017). However, since remyelination is often incomplete, research tools to investigate oligodendroglial dynamics and roles during the processes of demyelination and remyelination are of great importance for the development of therapeutic strategies.

It is now established that oligodendroglial Ca^{2+} signals translate environmental information into cellular processes such as proliferation, differentiation and myelination but little is known about the origin, dynamics or function of Ca^{2+} signals during myelin repair (Paez & Lyons, 2020; Pitman & Young, 2016; Maas et al., 2021). Recent *in vivo* studies in the zebrafish revealed that both OPCs and OLs are capable of Ca^{2+} signaling (Baraban et al., 2018; Krasnow et al., 2018; Marisca et al., 2020; Li et al., 2022). In mouse brain slices, spontaneous Ca^{2+} activity in OPCs (Balia et al., 2017) and OLs (Battefeld et al., 2019) was shown to be high during postnatal development when the myelination process is still ongoing, and to decrease in OLs as the brain matures (Battefeld et al., 2019). Then, Ca^{2+} signals of OLs are reactivated upon demyelination in the adult mouse brain, suggesting a crucial role for oligodendroglial Ca^{2+} signals in demyelinated lesions (Battefeld et al., 2019). To date, however, only one report has explored OL Ca^{2+} signaling during demyelination in *ex vivo* mouse brain slices (Battefeld et al., 2019) and oligodendroglial Ca^{2+} imaging studies in demyelinated mouse models *in vivo* are completely lacking. Moreover, in the above-mentioned studies, not only were the regions of interest (ROIs) manually chosen, potentially introducing bias in the ROI selection outcome, but also complex Ca^{2+} events with multiple peaks were overlooked even though these events are a hallmark of oligodendroglia (see below).

3

61   Several pipelines for the analysis of Ca^{2+} imaging data from neurons and astrocytes in brain slices

62   and *in vivo* have been published. Unfortunately, problems arise when using neuron-oriented programs

63   such as CaImAn and EZCalcium for the analysis of oligodendroglial Ca^{2+} imaging data (Cantu et al., 2020;

64   Giovannucci et al., 2019). For instance, classifiers are used to recognize neurons as round somata of a

65   certain size (Giovannucci et al., 2019), while oligodendroglia possess less well-defined shapes and sizes

66   (Xu et al., 2021). Another important drawback of the available pipelines for neuronal Ca^{2+} imaging is the

67   difference in neuronal and oligodendroglial Ca^{2+} signal dynamics. Indeed, neuronal Ca^{2+} signals last around

68   100 ms, are characterized by fast kinetics and occur with a high frequency (Chua & Morrison, 2016). This

69   is in stark contrast with oligodendroglia that exhibit complex Ca^{2+} dynamics with signals that last anywhere

70   from several seconds to multiple minutes and that are characterized by slow rise and decay times (our

71   data and Battefeld et al., 2019). Another set of problems may arise when using available Ca^{2+} imaging

72   analysis for astrocytes in oligodendroglia: astrocytes are known to exhibit extensive signal propagation

73   within and between cells and Ca^{2+} signaling pipelines such as AQuA are therefore designed to trace Ca^{2+}

74   events in time and space instead of identifying ROIs (Wang et al., 2019). Because we cannot assume that

75   intra- and inter-cellular signal propagation occurs extensively in oligodendroglia, these pipelines are not

76   immediately suitable for the analysis of oligodendroglial Ca^{2+} signaling. Older ROI-based astrocyte Ca^{2+}

77   imaging analysis packages such as GECIquant and CaSCaDe rely on manual input which may introduce

78   bias, making them not fully desirable (Agarwal et al., 2017; Venugopal et al., 2019).

79   Here, we provide a comprehensive experimental and analytical workflow to investigate

80   oligodendroglial Ca^{2+} imaging data obtained either *ex vivo* or *in vivo* in two different preclinical mouse

81   models of myelin repair, the lysolecithin (LPC) and cuprizone (CPZ) models. We established reproducible

82   experimental protocols aiming to obtain Ca^{2+} imaging data of oligodendroglia both in brain slices and in

83   freely moving mice expressing genetically encoded fluorescent Ca^{2+} indicators. Next, we developed two

84   free, open source and cross-platform software programs, Occam and post-prOccam (Occam:

85   Oligodendroglial cells calcium activity monitoring), for the fully automated analysis of one- and two-

86   photon Ca^{2+} imaging data from oligodendroglia in demyelinated lesions (GNU GPLv3+ license; code

87   repository at: *https://gitlab.com/d5674/occam*). These highly versatile and accessible tools are suitable

88   for the analysis of Ca^{2+} imaging datasets obtained in diverse preparations, matching all the specific

89   requirements for the monitoring of the unique Ca^{2+} event characteristics of oligodendroglia. Our analytical

90   pipeline thus accelerates the elucidation of Ca^{2+}-mediated mechanisms underlying myelin repair and will

91   contribute to the development of therapeutic strategies in myelin-related disorders such as MS.
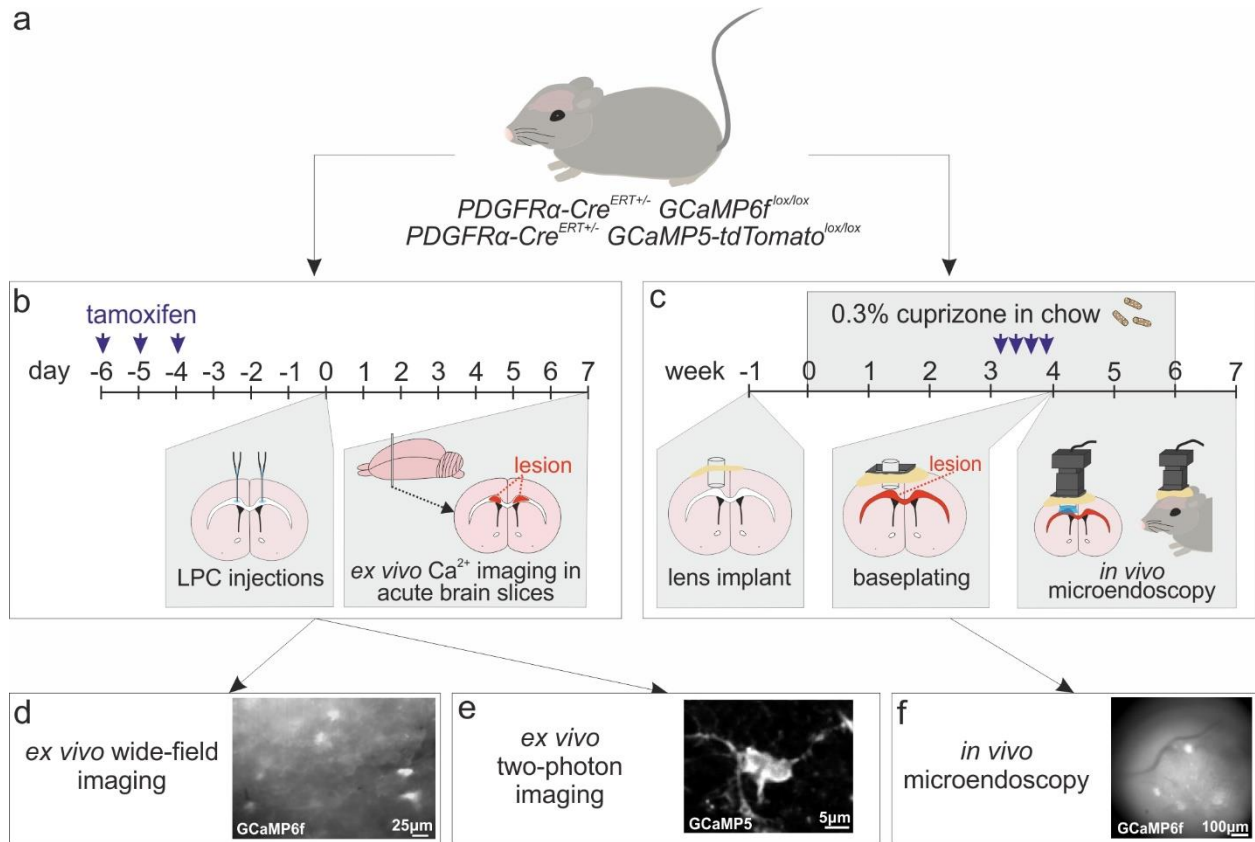
92   **Results**

93   **Experimental paradigms to obtain *ex vivo* and *in vivo* oligodendroglial Ca²⁺ signals in demyelinated**

94   **lesions**

95   The goal of this study was to develop both experimental paradigms and a fully automated

96   analytical workflow for the investigation of one- and two-photon intracellular Ca²⁺ imaging data from

97   oligodendroglia in demyelinated lesions of *ex vivo* and *in vivo* preparations (Fig. 1). We validated our

98   experimental and analytical workflow on data obtained in adult $Pdgfr\alpha^{CreERT(+/-)};Gcamp6f^{Lox/Lox}$ and

99    $Pdgfr\alpha^{CreERT(+/-)};Gcamp5\text{-}tdTomato^{Lox/Lox}$ transgenic mice (Fig. 1a). Ca²⁺ imaging in acute slices was

100   performed in LPC-induced lesions of corpus callosum as these lesions have several advantages: 1) since

101   these are focal lesions, they are localized in specific regions, 2) they can easily be identified by DIC video

102   microscopy at a low magnification as a brighter area than the surrounding non-lesioned dark-appearing

103   white matter (Sahel et al., 2015) and imaging can then be performed at a high magnification inside the

104   core of the lesion by either one- or two-photon Ca²⁺ imaging (Fig. 1b, 1d, 1e). In the LPC model, the

105   response of oligodendroglia to demyelination occurs in a stepwise manner (migration of OPCs to the

106   lesion site, OPC proliferation, OPC differentiation and remyelination), such that Ca²⁺ signals of

107   oligodendroglia at each step of the remyelination process can be analyzed separately (Sahel et al., 2015).

108   Tamoxifen injections to induce Cre expression a few days before the stereotaxic LPC injection are

109   sufficient to elicit a good level of GCaMP expression in oligodendroglia 7 days post-injection (dpi) of LPC

110   (Fig. 1b, 1d, 1e). This protocol led to a lesion-specific expression of GCaMP, as none was observed in intact

111   corpus callosum, probably because adult PDGFRα⁺ oligodendrocyte progenitors revert to an immature

112   state and shorten their cell cycle upon demyelination (Supplementary Fig. 1; Moyon et al., 2015; Cayre et

113   al., 2021). In this work, we imaged oligodendroglia in *ex vivo* demyelinated brain slices by two different

114   techniques: one-photon microscopy used to study the whole oligodendroglial population's Ca²⁺ activity in

6

115   a wide field and conventional two-photon microscopy used to study the oligodendroglial Ca^{2+} signals at

116   the single cell level (Fig. 1b, 1d, 1e).

117
118

Figure 1 – Experimental workflow for oligodendroglial Ca^{2+} imaging of *ex vivo* and *in vivo* preparations.
(a) Demyelinating lesions were performed in adult *Pdgfra$^{CreERT(+/-)}$;Gcamp6f$^{Lox/Lox}$* and *Pdgfra$^{CreERT(+/-)}$;Gcamp5-tdTomato$^{lox/Lox}$* transgenic mice. **(b)** Four days after tamoxifen injection, demyelination was induced by LPC injection in the corpus callosum and *ex vivo* brain slices were performed 7 days after LPC injection. **(c)** Demyelination was induced by CPZ ingestion starting 1 week after GRIN lens implantation and tamoxifen injections were performed during the fourth week of CPZ ingestion. *In vivo* microendoscopy was performed from the fifth week of CPZ feeding and during the first week after CPZ withdrawal. **(d-f)** Ca^{2+} imaging in lesions was performed using wide-field microscopy (d) and two-photon microscopy (e) in *ex vivo* brain slices and wide-field microendoscopy (f) in freely moving mice.

128

129   After successfully imaging the Ca^{2+} dynamics in demyelinated lesions in *ex vivo* brain slices, we

130   extended our approach by including *in vivo* Ca^{2+} imaging in demyelinated lesions. The main difficulty

131   encountered when imaging the mouse corpus callosum *in vivo* is related to the depth of this region,

132   particularly at the level of the motor cortex where demyelinated lesions are often analyzed (Ortiz et al.,

7

133   2019). Although some lesions occur in the grey matter in MS, most of them actually occur in the white

134   matter; therefore, performing oligodendroglial Ca^{2+} imaging in corpus callosum lesions is particularly

135   relevant for this disease. For this purpose, we used *in vivo* one-photon microendoscopy which allowed us

136   to visualize Ca^{2+} signals of oligodendroglia in the corpus callosum, at 1.8 mm from the surface of the brain.

137   In order to monitor oligodendroglial Ca^{2+} signaling in callosal demyelinated lesions of freely moving mice

138   (Fig. 1c), we operated the open-source Miniscope V4 device, often used to follow neuronal Ca^{2+} activity

139   (Shuman et al., 2020; Cai et al., 2016). One interesting challenge in our approach was the fact that,

140   although the LPC-induced demyelination model is appropriate for brain slices, demyelination is already

141   obtained at 3 dpi (Sahel et al., 2015) and thus incompatible with *in vivo* microendoscopy which requires a

142   multi-step procedure extending over several weeks (Fig. 1c). We therefore used the CPZ demyelination

143   model in which intense demyelination occurs from the fourth week after CPZ ingestion without any

144   surgical intervention (Fig. 1c; Remaud et al., 2017). For these experiments, a GRIN lens was implanted

145   deep in the cortex above the target imaging region seven days before the start of the CPZ treatment. Five

146   weeks after the GRIN lens implantation, a baseplate was mounted onto the animal's skull providing

147   fixtures to attach the Miniscope and allowing us to set the working distance between the objective and

148   the lens (Fig. 1c). The tissue can thus recover for five weeks and any inflammation or blood accumulation

149   under the lens can be cleared before the beginning of Ca^{2+} imaging experiments (Zhang et al., 2019).

150   Tamoxifen was injected during the fourth week of CPZ treatment, when demyelination is advanced.

151   Finally, *in vivo* imaging was done during demyelination to record Ca^{2+} signals from oligodendroglia in the

152   demyelinated corpus callosum of freely moving mice (Fig. 1c, 1f).
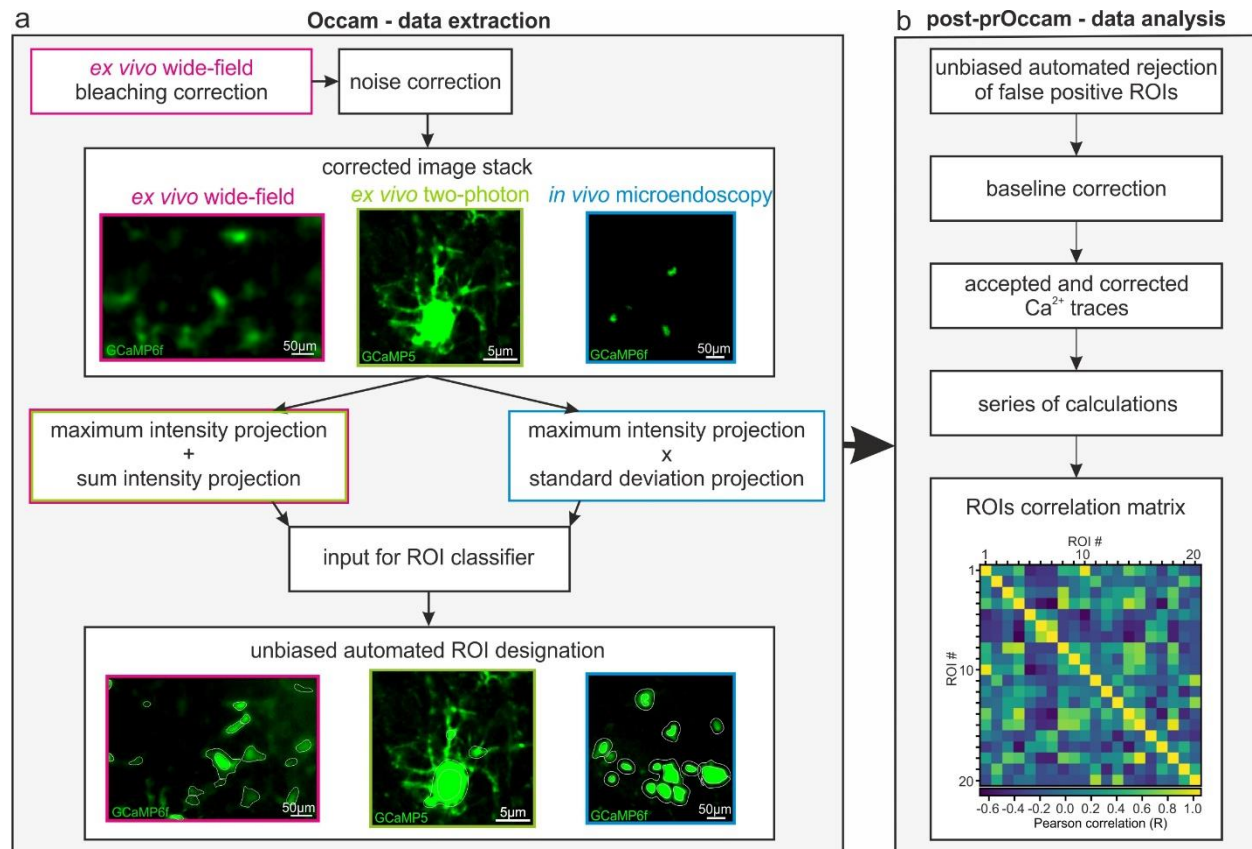
153

154

155

8

156 **Occam and post-prOccam: Ca²⁺-signal analysis softwares for investigation of oligodendroglia in**

157 **demyelinated lesions**

158   To perform an automated and unbiased detection of active regions in different Ca^{2+} imaging

159 datasets from demyelinated preparations, we developed a configurable Fiji/ImageJ2 plugin named Occam

160 (Oligodendroglial cells calcium activity monitoring; Fig. 2a). We first validated our analytical workflow on

161 wide-field one-photon Ca^{2+} imaging data recorded in acute slices of corpus callosum which revealed high

162 levels of spontaneous Ca^{2+} activity in oligodendroglia of LPC-induced demyelinated lesions (Fig. 1b, 1d, 2a,

163 3a; Supplementary Video 1). Occam first performs noise and bleaching corrections of image stacks (Fig.

164 2a) and then uses the trainable machine learning-based WEKA Fiji/ImageJ2 segmentation plugin (Arganda-

165 Carreras et al., 2017) combined with a local maxima segmentation tool to define regions of interest (ROIs)

166 with fluctuating Ca^{2+} signals with high and medium pixel intensities (Supplementary Manual). Several

167 parameters of ROI detection can be configured by the user to optimize Occam's performance and to

168 obtain an automated and unbiased ROI designation (for instance, the minimum size of an active ROI or a

169 bleaching correction option). Once the ROI designation process is completed, Occam saves two files: one

170 file stores each ROI area size in pixels and the coordinates of the geometric center of the ROI, the other

171 file describes each ROI's fluorescence behavior over time as a vector listing the mean fluorescence pixel

172 intensity value in each frame contained in the image stack. The ROI fluorescence intensity vector is also

173 referred to as the ROI trace (Supplementary Fig. 2a, 2b; Supplementary Manual). These two files are then

174 read by the post-prOccam software to perform a systematic ROI analysis along with quantitative

175 calculations ultimately aimed at easing the detailed characterization of oligodendroglial Ca^{2+} activity (Fig.

176 2b). The post-prOccam software was implemented as a configurable program where users can set various

177 analysis parameters in a configuration file so as to adapt its operation to any specific dataset

178 (Supplementary Manual).

Figure 2 – Occam and post-prOccam: an open source, fully automated and configurable analysis toolkit for oligodendroglial Ca²⁺ imaging of *ex vivo* and *in vivo* preparations. (a) The Occam software is available as a Fiji (tested in version 1.53t and earlier) plugin and configurable for the analysis of wide-field, two-photon and *in vivo* microendoscopy Ca²⁺ imaging. Occam performs bleaching correction only on *ex vivo* wide-field image stacks and does noise correction according to imaging condition (Supplementary Manual). Then, it uses the maximum and sum intensity projections for *ex vivo* image stacks and the maximum and standard deviation projections for *in vivo* image stacks to build an input for the ROI classifier. The ROI classifier of Occam defines ROIs with significant Ca²⁺ fluctuations fully automated and is used by WEKA for ROI designation. **(b)** Output of Occam can be fed to post-prOccam which is a configurable Python-based software that first rejects any ROIs that do not show significant Ca²⁺ fluctuations, then performs baseline corrections, subsequently performs a series of calculations for each ROI in the image stack and finally computes a ROIs correlation matrix of the Pearson correlation value of each ROI as compared to every other ROI. Occam and post-prOccam are available as free, multiplatform and open source softwares at: *https://gitlab.com/d5674/occam* and procedures are described in more detail in the Supplementary Manual.
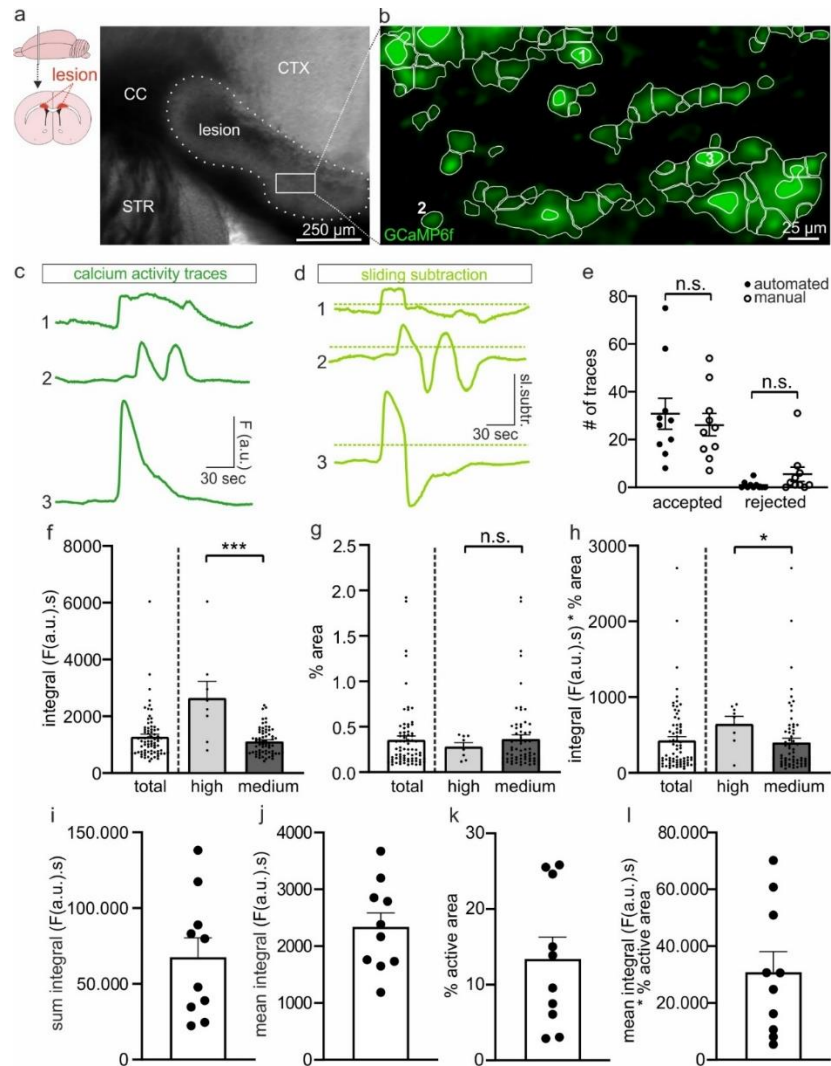
Automated ROI detection algorithms cannot be error-free and almost always require an *a posteriori* rejection of false positive ROIs (Cantu et al., 2020). We developed the post-prOccam program that automatically fetches the data written by Occam and proceeds to an automatic rejection of ROIs lacking significant Ca²⁺ signal fluctuations. To reject false positive ROIs, we adapted an algorithm

200 previously used for the fluorescence-based tracking of exocytotic events (Yuan et al., 2015; Supplementary Manual). Based on repeated intensity values subtraction in a sliding window over the whole ROI vector of mean intensity values (Supplementary Fig. 2a-c), our method allowed us to single out fluorescence intensity changes in an image stack that were greater than noise fluctuations (Fig. 2b, 3a-d). Since Ca^{2+} signals of oligodendroglia in lesions were characterized by long-lasting kinetics (Fig. 3c; rise time: 54.63±9.67 frames, equivalent to 35.25±5.36 s, n=34 events from n=8 fields), the sliding window subtractions were computed between points distanced by 40 frames, as: intensity = intensity(ROI[n+40]) - intensity(ROI[n]), with n being the frame number in the stack (Supplementary Fig. 2b, 2c). Each initial ROI trace is thus replaced by a new one, as computed from the sliding window subtractions, that is then tested against user-defined threshold parameters set in the configuration file (Fig. 3d; Supplementary Files 1-3). These threshold settings configure the rejection of ROI traces depending on both their Ca^{2+} event kinetics and noise. To find the best settings to eliminate false positive traces, we empirically changed the threshold parameters and compared the results with those obtained by a manual rejection of ROIs in several imaging stacks (Fig. 3e). The threshold values that were found to be the most effective in rejecting false positive ROIs were set as default values in the configuration file and provided in Supplementary File 1 (Fig. 3e; see detailed description of the threshold parameters in the Supplementary manual).

Once the accepted ROIs have been selected, post-prOccam performs a baseline subtraction for each ROI trace by subtracting a mean minimum intensity value previously calculated from a configurable number of trace points (Supplementary File 1; Supplementary Manual). We used a baseline subtraction computation rather than the conventional $[(F(t)-F_0)/F_0]$ computation because we adapted the analysis to the Ca^{2+} dynamics of oligodendroglia in lesions. Indeed, the oligodendroglial cells studied in this report exhibited high overall levels of spontaneous Ca^{2+} activity, often right at the start of the recording, making it difficult to determine with certainty the F_0 value of the resting fluorescence intensity. Finally, the post-prOccam program performs a series of calculations to help characterize the Ca^{2+} activity of oligodendroglia

224   in lesions (Fig. 2b). Figure 3f-h illustrates part of the calculations performed for each ROI in a single image

225   stack, *i.e.* the mean integral, the percentage of active area and the mean integral multiplied by the

226   percentage of the active area. Since the complex features of oligodendroglial Ca^{2+} events preclude their

227   proper individual isolation (Supplementary Fig. 3), we found it more appropriate to calculate the mean

228   intensity integral of each ROI trace rather than to use a procedure for single event detection (see

229   discussion). As expected, high intensity ROIs exhibited significantly larger mean integrals than medium

230   intensity ROIs (Fig. 3f) and, despite similar mean percentage of active area between high and medium

231   intensity ROIs, the mean integral multiplied by the percentage of the active area remained larger for high

232   intensity ROIs (Fig. 3g-h). However, when considering all the analyzed stacks, the number of high intensity

233   ROIs was always largely smaller than the number of medium intensity ROIs (3.5±0.9 high intensity ROIs,

234   n=27.3±5.7 medium intensity ROIs and n=30.8±6.5 total ROIs for n=10 stacks). Moreover, the mean

235   integral of medium intensity ROIs and that of all pooled data (Total) remain similar (Fig. 3f). Therefore, we

236   hereinafter pooled the data from high and medium intensity ROIs for quantifications, but kept their

237   detection separate because the WEKA plugin used by Occam performed better when classifying ROIs in

238   these two categories. The average calculations for all ROIs in several image stacks show that Ca^{2+} activity

239   between demyelinated lesions at 7 dpi can be variable but sufficiently high to always allow us to detect

240   changes over only a few minutes of recording (Fig. 3i-l).

12

241

Figure 3 – Using Occam and post-prOccam for analysis of ex vivo wide-field oligodendroglial Ca²⁺ imaging from a callosal LPC-induced demyelinated lesion. (a and b) Representative image of a demyelinated lesion in 4x DIC microscopy (a) and of GCaMP6f expressing oligodendroglia in 40x wide-field fluorescence imaging displaying detected active ROIs (white) as obtained with Occam (b). **(c and d)** Representative corrected ROI traces (c) and sliding window subtraction traces (d) as obtained with post-prOccam. **(e)** Comparison of the manual rejection of false positive ROIs and the automatic rejection of false positive ROIs by post-prOccam revealed no differences in accepted and rejected ROIs, validating post-prOccam's performance. n.s.: not significant, two-way ANOVA followed by a Bonferroni multiple comparisons test. **(f-h)** Calculations performed by post-prOccam on each individual ROI of the image stack include amongst others the integral (f), percentage of active area (g) and integral multiplied by percentage of active area (h) and are separated for high and medium intensity ROIs. *p<0.05 and ***p<0.001; Mann-Whitney test. **(i-k)** Calculations performed by post-prOccam on all ROIs in an image stack include amongst others the sum integral (i), the mean integral (j), the percentage active area (k) and the mean integral multiplied by the percentage active area (l) (n=10 stacks, n=10 slices, n=7 mice). Error bars represent standard error of the mean. Dot plots are presented as mean±s.e.m.
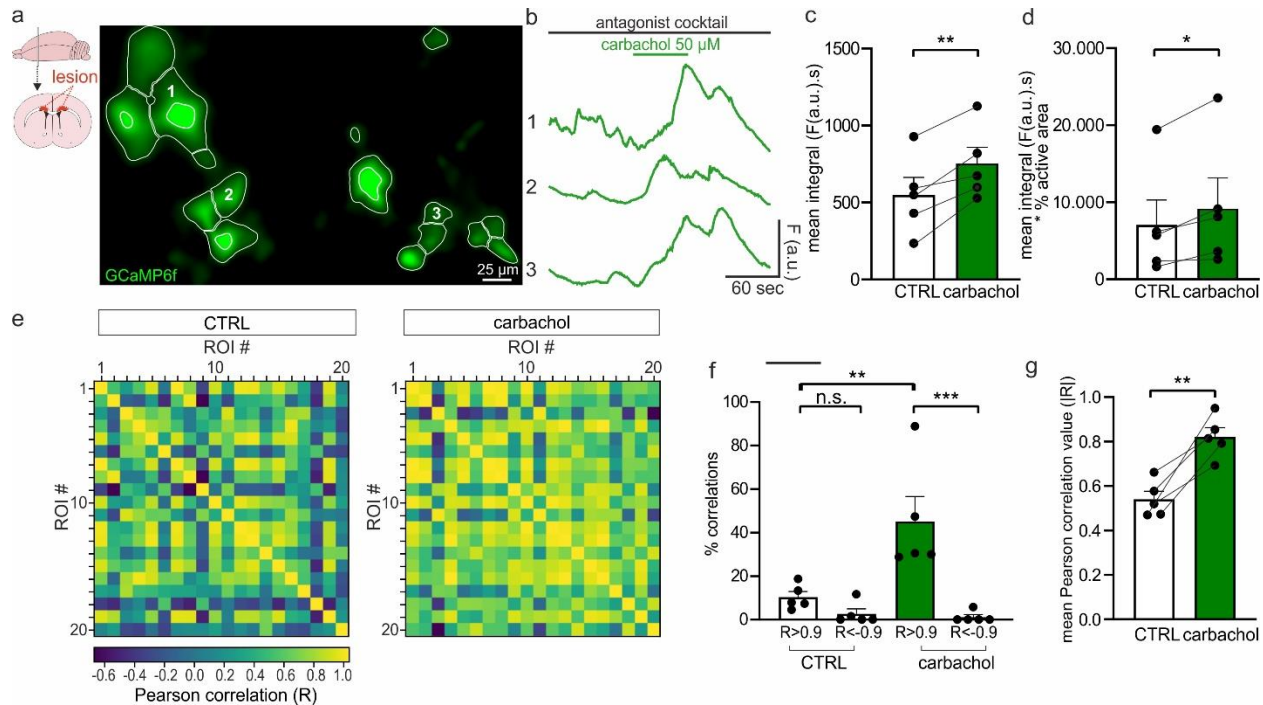
257

13

258   For informational and debugging purposes, a log file is produced by post-prOccam with a highly

259   detailed account of all the data processing steps and their outcome. The accepted ROIs and the

260   corresponding processed data of a stack are saved by post-prOccam in two separate files for further

261   statistical analysis. Of note is the pp-supervisor program that allows the scientist to run post-prOccam

262   automatically over a set of stacks located in a single directory using the configuration file that was

263   elaborated during the exploratory steps described above.

264

265   **Interval-based analysis and evaluation of synchronized Ca^{2+} signals of oligodendroglia in lesions**

266   One important feature of post-prOccam is its ability to compare ROIs only at specific time point

267   intervals of the recorded datasets. For instance, in the case of applications of pharmacological agents

268   during Ca^{2+} imaging recordings, a user might wish to compare Ca^{2+} signals in the absence or in the presence

269   of a drug in a single image stack. The default post-prOccam software behavior is to perform all the

270   calculations described in the previous sections on the whole ROI vector. However, in specific cases

271   mentioned above, it might be useful for the calculations to be performed only over selected ranges of the

272   ROI vector (that is, intervals of that ROI's acquisition time points). The configuration file provides a section

273   in which the user might list any number of ROI vector intervals over which to perform the previously

274   described calculations. To validate this feature, we bath-applied the muscarinic receptor agonist

275   carbachol in the presence of a cocktail of antagonists to stimulate intracellular Ca^{2+} signals of

276   oligodendroglia during one-photon Ca^{2+} imaging recordings of 7 dpi callosal LPC-induced lesions in brain

277   slices (Fig. 4a, 4b). Oligodendroglia express muscarinic receptors M1, M3 and M4, which, when activated

278   by carbachol, increase intracellular Ca^{2+} signals (Abiraman et al., 2015; Cohen & Almazan, 1994; Welliver

279   et al., 2018). In order to determine the extent of the Ca^{2+} signal activity changes upon the bath application

280   of carbachol, we directed post-prOccam to compare the Ca^{2+} signals in each ROI only during two distinct

281   acquisition intervals: the control interval before the carbachol application and the interval during which

14

282   the carbachol was applied. As expected, we observed that a bath application of 50 µM carbachol in the

283   presence of a cocktail of antagonists indeed induced an increase in intracellular Ca²⁺ signals in

284   oligodendroglia, as revealed by an increase in both the mean integral and the mean integral multiplied by

285   the percentage of the active area, compared to the control (Fig. 4a-d).

286

287

288   **Figure 4 – Using Occam and post-prOccam for interval analysis and evaluation of synchronized Ca²⁺**
289   **signals of oligodendroglia in LPC-induced demyelinated lesions. (a)** Representative image of Ca²⁺ imaging
290   in callosal LPC-induced lesions in *ex vivo* brain slices that were exposed to 50 µM carbachol to induce
291   increases in Ca²⁺ signals in oligodendroglia in the presence of an antagonist cocktail containing 10 µM
292   NBQX, 50 µM AP5, 10 µM GABAzine, 1 µM TTX and 50 µM mecamylamine. The image displays detected
293   active ROIs (white) as obtained with Occam. **(b)** Representative Ca²⁺ traces showing Ca²⁺ increases during
294   carbachol application as obtained with post-prOccam. **(c and d)** Mean integral (c) and mean integral
295   multiplied by the percentage of active area (d) of Ca²⁺ signals in control and after exposure to carbachol.
296   *p<0.05, **p<0.01; paired Student's t-test. **(e)** Example of correlation matrixes obtained with post-
297   prOccam before and after carbachol exposure. Each square indicates the Pearson correlation value of one
298   ROI with another. Yellow indicates high positive Pearson correlation, while dark blue indicates high
299   negative correlations. Note that traces 1, 2, 3 in b correspond to ROIs 7, 12, 14 in the matrix. **(f)** The
300   percentage of correlations in the correlation matrix that is significantly negative (R<-0.9) or significantly
301   positive (R>0.9) in both control and carbachol exposed conditions. n.s.: not significant, **p<0.01,
302   ***p<0.001, two-way ANOVA followed by a Tukey's multiple comparisons test. **(g)** Mean Pearson
303   correlation values for control and carbachol conditions. CTRL: control before carbachol exposure (n=5
304   stacks, n=5 slices, n=4 mice). **p<0.01; paired Student's t-test. Dot plots are presented as mean±s.e.m.

15

305

306   While it is now established that a population of astrocytes may exhibit high levels of synchronized

307   Ca^{2+} activity *in vitro* and *in vivo* (Kolzumi et al., 2010; Ingiosi et al., 2020), nothing is known about the

308   potential of Ca^{2+} signals in oligodendroglia to be synchronized. We thus tested this possibility in

309   demyelinating lesions by implementing a correlation calculation which allows the user to establish

310   whether ROIs within a given image stack show synchronized Ca^{2+} signals. The post-prOccam program

311   computes an inter-ROI Pearson correlation coefficient matrix between each ROI trace and every other ROI

312   trace (Fig. 4e; see Materials and Methods; Ingiosi et al., 2020). In control conditions, we found that most

313   ROIs did not show any correlated Ca^{2+} activity, as evidenced by a low percentage of correlated ROIs (|R|

314   < 0.9) and a mean Pearson correlation coefficient R value of 0.54±0.24 (Fig. 4f-g). The remaining few ROIs

315   that displayed correlated Ca^{2+} activity had mainly a positive rather than a negative correlation (Fig. 4f).

316   Interestingly, upon application of the muscarinic agonist carbachol in the presence of a cocktail of

317   antagonists, a significant overall increase of the positive inter-ROI Ca^{2+} activity correlation was observed

318   (Fig. 4e-g), with a mean Pearson correlation value of 0.82±0.04. These data showed that the majority of

319   ROIs did simultaneously respond to the agonist. The post-prOccam software thus successfully determined

320   the degree of Ca^{2+} activity correlation between ROIs and was able to detect simultaneous increases of

321   that activity as induced by pharmacological agents. In order to adapt to any specifics of biological

322   applications, the Pearson correlation R value threshold might be configured. The percentage of correlated

323   ROIs as well as the mean Pearson correlation coefficient are reported for each image stack in the

324   corresponding output file generated by the program. Taken together, our results show that the Occam

325   and the post-prOccam software programs make for a configurable and automatable solution for the

326   analysis of oligodendroglial Ca^{2+} signals.
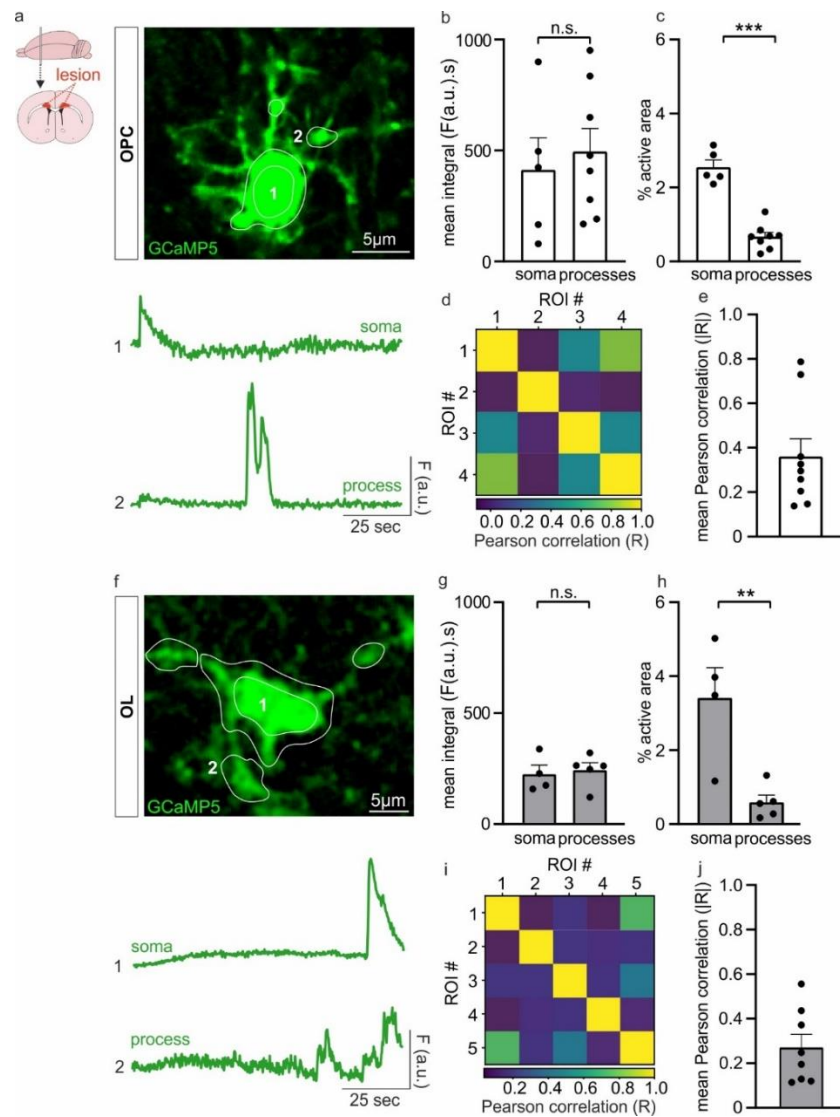
327

328

329   **Two-photon imaging of Ca²⁺ signals in single oligodendroglia in demyelinated lesions**

330   Although one-photon imaging allows one to determine the global Ca²⁺ signaling properties of

331   oligodendroglia in a large area of the LPC-induced lesion, the spatial resolution of this technique is not

332   sufficient to reveal local Ca²⁺ changes occurring specifically either in the soma or in the cell processes of

333   any individual cell. To test whether our workflow is suitable for the analysis of images obtained by two-

334   photon microscopy at the single cell resolution, we performed two-photon Ca²⁺ imaging of putative OPCs

335   and OLs in callosal LPC-induced lesions in *ex vivo* brain slices and analyzed the data using Occam and post-

336   prOccam (Fig. 5; Supplementary Video 2 and Supplementary File 2). We used morphological criteria to

337   distinguish OPCs and OLs, and only recorded cells for which we could connect the processes to a particular

338   soma. In corpus callosum, OPCs were characterized by a relatively small round soma and a stellate

339   arborization with thin processes (Fig. 5a; Chittajallu et al., 2004) whereas OLs had a larger soma and

340   principal processes often aligned with axons (Fig. 5f; Bakiri et al., 2011). Morphological determination of

341   putative OPCs and OLs allowed us to reveal that, even though the area of ROIs in the processes is

342   significantly reduced as compared to that of ROIs in the soma, the mean intensity integral of their Ca²⁺

343   signals is similar to that of Ca²⁺ signals from the cell soma (Fig. 5a-c, 5f-h). Although the mean number of

344   ROIs in OPCs and OLs was similar (9.44±1.97 in OPCs vs 8.00±2.19 in OLs) as was the rise time of Ca²⁺

345   events (3.61±1.14 s n=10 events from 5 fields for OPCs vs 4.16±0.68 s; n=37 events from 6 fields for OLs

346   p=0.71 for soma and process data pooled together, unpaired Student's t-test), Ca²⁺ signals had a higher

347   integral in OPCs than in OLs (Fig. 5 a-c, 5f-h, p=0.0391 for soma and process data pooled together,

348   unpaired Student's t-test)). Altogether, these results not only show high levels of Ca²⁺ activity in processes

349   of OPCs and OLs, but also that this activity is greater in OPCs inside demyelinating lesions. Importantly,

350   we also observed that, whatever the cell type involved (OPCs or OLs), the Ca²⁺ signals were poorly

351   correlated, which suggests that they occurred independently in the soma and in the processes and at

352   different subcellular locations (Fig. 5 d-e, 5i-j). In summary, these results show that Occam and post-

17

353 prOccam can successfully determine the characteristics of oligodendroglial Ca²⁺ signals recorded by

354 different imaging techniques and at different spatial scales.

355

Figure 5 – Using Occam and post-prOccam for the analysis of two-photon oligodendroglial Ca²⁺ imaging in callosal LPC-induced demyelinated lesions in *ex vivo* brain slices. (a) Representative image of a putative OPC **(a)** and a putative OL **(f)** expressing GCaMP5 with examples of corrected Ca²⁺ traces from the soma and a process (bottom) obtained with Occam and post-prOccam. **(b-c, g-h)** Mean integrals (b, g) and % active area (c, h) for the soma and the processes of OPCs (b-c) and OLs (g-h). n.s.: not significant. **p<0.01, ***p<0.001, unpaired Student's t-test. **(d, i)** Examples of correlation matrices describing a lack of synchronization of Ca²⁺ signals in the soma and processes of OPCs (d) and OLs (i). Each square indicates the Pearson correlation value of one ROI with another ROI. Yellow indicates high positive Pearson correlation, while blue indicates no correlation. Note that traces 1 and 2 in a and f correspond to ROIs 1, and 2 in the matrices in d and i, respectively. **(e and j)** The mean correlation value of OPCs and OLs (n=9 stacks, n=9 slices, n=7 mice for OPCs and n=8 stacks, n=7 slices, n=6 mice for OLs). Dot plots are presented as mean±s.e.m.

18

368 ***In vivo* microendoscopy Ca^{2+} imaging of oligodendroglia during the demyelination process**
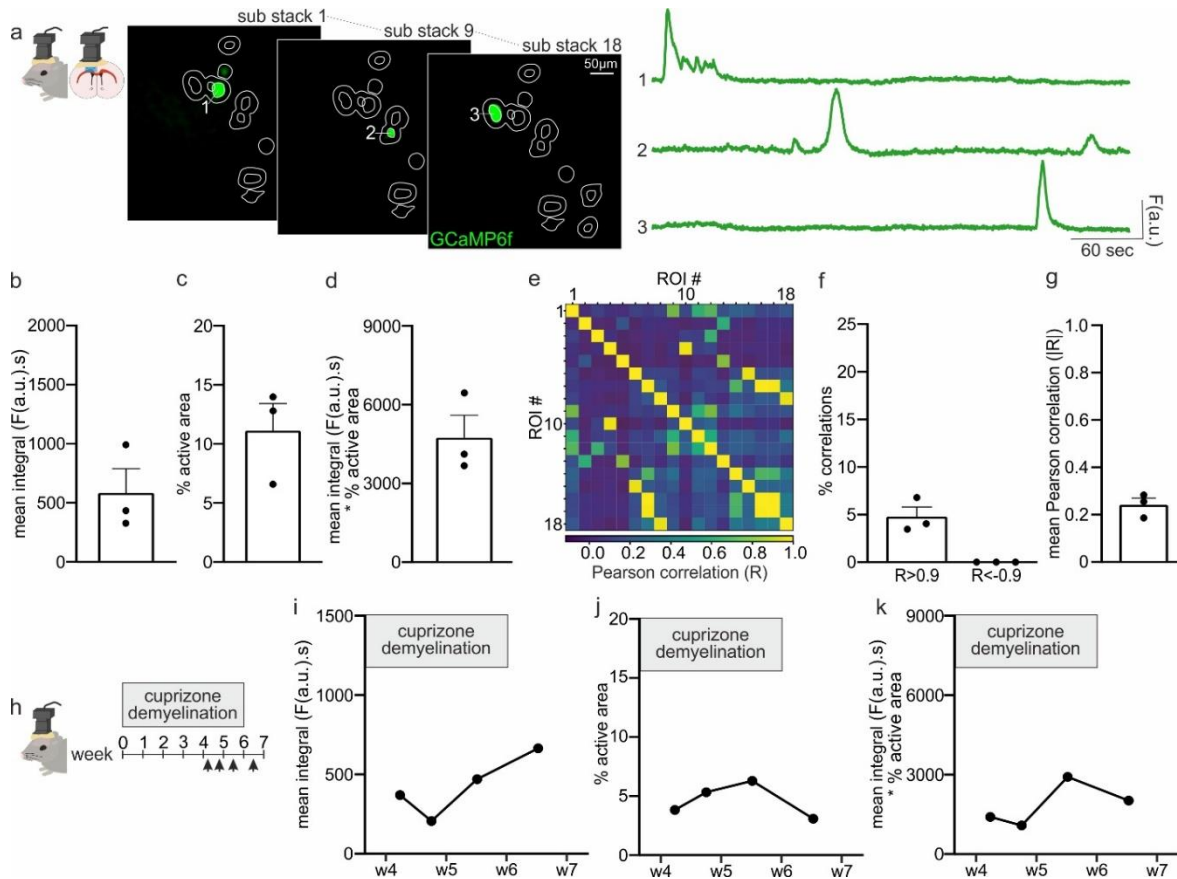
369   Although *in vivo* Ca^{2+} imaging has been extensively studied in neurons and astrocytes, only few

370 studies in the zebrafish have reported *in vivo* Ca^{2+} signals in oligodendroglia (Baraban et al., 2018; Krasnow

371 et al., 2018; Marisca et al., 2020; Li et al., 2022). Moreover, no current information exists on

372 oligodendroglial Ca^{2+} imaging in the demyelinated mouse brain *in vivo*. To fill this gap, we decided to adapt

373 our experimental and analytical workflow to the study of oligodendroglial Ca^{2+} signals during

374 demyelination in freely moving mice (Fig. 1c-f, Fig. 2a). As a proof-of-concept, we used the CPZ-induced

375 demyelination model and performed microendoscopic Ca^{2+} imaging recordings of oligodendroglia in the

376 corpus callosum of awake demyelinated mice (Fig. 6a-b; Supplementary Video 3). Four animals were

377 implanted according to the procedure described in Figure 1. Three of them were recorded during the fifth

378 postnatal week of CPZ feeding, when demyelination is advanced (Remaud et al., 2017), and sacrificed

379 afterwards in order to confirm the proper position of the GRIN lens above the corpus callosum. The fourth

380 mouse was maintained alive and imaged at four different timepoints to show that multiple recordings of

381 the same animal can be made over several weeks.

382   The image stacks we acquired contained 4200 frames collected over 7 minutes. To enhance the

383 precision of ROI detection by Occam in such large data files, the program first splits the image stack into

384 a configurable number of sub-stacks. Then, for each sub-stack, it performs the noise correction, uses the

385 maximum and standard deviation projections to build an input for the ROI classifier and proceeds to the

386 automated ROI designation using the WEKA Fiji/ImageJ2 segmentation plugin combined with a local

387 maxima segmentation tool (Fig. 2a; Supplementary Manual). This side-step from the *ex vivo* version of

388 Occam allows for accurate detection of ROIs in large image stacks collected over many minutes because

389 it also captures ROIs that are only briefly active and that would be overlooked when making a projection

390 image over the entire imaging duration. However, this procedure can lead to an overestimation in the

391 number of active ROIs if a specific region of the stack is active several times during a single experiment

392   and, thus, is detected as a ROI in multiple sub-stacks. To overcome this problem, Occam projects all ROIs

393   from all sub-stacks onto each other and allows the user to determine a degree of overlap for which

394   overlapping ROIs are merged into a single ROI (Supplementary Manual). Like for *ex vivo* preparations, ROIs

395   with high and medium pixel intensities were considered as displaying significant Ca^{2+} signal fluctuations.

396   As the number of sub-stacks can be configured by the user, the ROI detection process will be successful

397   even in recordings longer than 7 minutes, either in a single acquisition or in multiple acquisitions

398   performed on the same animal over weeks (Fig. 6). In sum, Occam features for in vivo experiments have

399   been adapted so that it can detect not only shortly occurring events, but also the repeated activation of a

400   single region over a long experiment. Once the ROI selection process has been performed, the

401   downstream processing by post-prOccam is identical to that described in the preceding sections

402   (Supplementary File 3).

403   Our analysis revealed that oligodendroglia *in vivo* show high levels of spontaneous Ca^{2+} activity in

404   the fifth week of CPZ-induced demyelination (Fig. 6a-d; mean number of ROIs of 15±4.58). We could

405   identify ROIs with multiple Ca^{2+} events with complex and long-lasting kinetics of several seconds (Fig. 6a

406   and Supplementary Fig. 3c). The mean rise time, however, was on average faster than in *ex vivo* wide-field

407   experiments (rise time: 31.48±5.54 frames, equivalent to 6.29±0.91 s, n=48 events from n=3 fields).

408   Furthermore, the low percentage of correlated ROIs and the small mean Pearson correlation coefficient

409   showed that most ROIs did not display any correlated Ca^{2+} activity (Fig. 6e-g), confirming the lack of

410   synchronized Ca^{2+} signals in oligodendroglia observed *ex vivo* in the LPC model. Finally, we performed *in*

411   *vivo* microendoscopy Ca^{2+} imaging in the same mouse during weeks 5 and 6 of CPZ-induced demyelination

412   and during week 7 after CPZ withdrawal (Fig. 6h). The mean pixel intensity integral, the percentage of

413   active area and the mean integral multiplied by the percentage of the active area remained relatively

414   stable during this period, indicating that the imaging conditions did not deteriorate over time (Fig. 6h-k).

415   The monitoring of oligodendroglial Ca^{2+} activity over weeks in the same animal may give insight into the

416 behaviour of this cell population during demyelination. To our knowledge, this is the first time that Ca^{2+}

417 signals of oligodendroglia during demyelination have been recorded in real time and the successful

418 validation of our workflow prompts future research on oligodendroglial Ca^{2+} signaling in the living injured

419 mammalian brain.

420

421 **Figure 6 – Using Occam and post-prOccam for the analysis of *in vivo* microendoscopy Ca^{2+} signals of**
422 **oligodendroglia in the demyelinated corpus callosum of freely moving mice. (a)** Representative images
423 and corrected Ca^{2+} traces of microendoscopy Ca^{2+} imaging in freely moving mice during the fifth week of
424 CPZ demyelination. The image displays detected active ROIs (white) in several sub-stacks as obtained with
425 the *in vivo* analysis option of Occam. **(b-d)** Mean integral (b), % of active area (c) and mean integral
426 multiplied by percentage of active area (d) during the fifth week of CPZ demyelination (n=3 mice). Data is
427 presented as mean±s.e.m. **(e)** Correlation matrix of the *in vivo* experiment in a obtained with post-
428 prOccam. Each square indicates the Pearson correlation value of one ROI with another ROI. Yellow
429 indicates high positive Pearson correlation, while dark blue indicates no Pearson correlation. Note that
430 trace 1, 2, 3 in a correspond to ROIs 1, 2, 3 in the matrix. **(f)** The percentage of correlations in the
431 correlation matrix. **(g)** The mean Pearson correlation value. **(h)** *In vivo* microendoscopy Ca^{2+} imaging was
432 performed in the same mouse at four timepoints, namely during weeks 5 and 6 of CPZ-induced
433 demyelination and during week 7 after CPZ withdrawal. **(i)** Mean integral, **(j)** % of active area and **(k)** mean
434 integral multiplied by percentage of active area during the fifth, sixth and seventh week in the same
435 mouse.

436   **Discussion**

437   While it is suspected that oligodendroglial Ca^{2+} signaling plays a key role in myelin repair, the

438   characteristics of oligodendroglial Ca^{2+} signals in demyelinated lesions remain unknown. This is due to a

439   limited number of *ex vivo* or *in vivo* Ca^{2+} imaging studies as well as a lack of automated analytical tools

440   adapted to the monitoring of the specific characteristics of oligodendroglial Ca^{2+} activity. To fill this need,

441   we devised experimental conditions for *ex vivo* and *in vivo* Ca^{2+} imaging in mouse demyelinated lesions

442   and implemented an analytical workflow comprising two programs, Occam and post-prOccam, which

443   provide a reliable solution for the automated in-depth analysis of one- and two-photon oligodendroglial

444   Ca^{2+} imaging data. Tested in Windows 10 and Debian GNU/Linux, these cross-platform programs were

445   designed to be easily configurable to ensure an unbiased selection of active ROIs and to allow an efficient

446   analysis of large datasets. Licensed under the GNU GPLv3+ license, both programs can be freely used,

447   modified according to any specific need and question, and redistributed. Since the Ca^{2+} signal detection is

448   finely configurable in both programs, the use of our software solution might be extended to new use cases

449   such as other glial cell types.

450   By harnessing the features in these two programs, we could monitor the spontaneous

451   oligodendroglial Ca^{2+} activity in different toxic models of demyelination, both *ex vivo* and *in vivo*. In any of

452   these possible configurations, Ca^{2+} traces that were first obtained with Occam then undergo a post-

453   processing procedure with post-prOccam that processes them to reject ROIs with too small Ca^{2+}

454   fluctuations (false positives), which can be construed as a refinement of the ROI detection process. We

455   found that this automatic Ca^{2+} trace selection in our workflow performs equally well as a manual Ca^{2+}

456   trace selection, thus validating the procedure. Among other analysis options, the ability to restrict the

457   processing and quantification steps to specific acquisition intervals has proven useful to screen the effect

458   of drugs on oligodendroglial Ca^{2+} signaling. Furthermore, a number of features in post-prOccam make it

459   possible to spot eventual synchronized Ca^{2+} signals across different ROIs in a given frame stack. Here we

22

460 successfully applied these analysis modalities to detect, quantify and correlate Ca^{2+} activity increases upon

461 carbachol bath application to demyelinated brain slices in order to activate muscarinic receptors in

462 oligodendroglia, as previously described in cell culture (Cohen & Almazan, 1994; Welliver et al., 2018).

463 Interestingly, muscarinic receptor agonists can increase OPC proliferation, but block OPC differentiation

464 and remyelination (De Angelis et al., 2012; Abiraman et al., 2015; Welliver et al., 2018). Moreover, the

465 muscarinic receptor antagonist benztropine was found to be beneficial to induce myelin repair in an

466 animal model (Deshmukh et al., 2013) and the muscarinic receptor antagonist clemastine was shown to

467 improve myelin regeneration in a clinical trial with multiple sclerosis patients (Green et al., 2017). The

468 positive effect of these antagonists might thus be caused by the blockade of muscarinic receptor-

469 dependent Ca^{2+} signaling mechanisms, which is a subject for further research. These studies highlight the

470 importance of investigating the Ca^{2+} response of oligodendroglia to novel remyelinating drugs. The

471 workflow described in this report will facilitate these future studies.

472 Oligodendroglial Ca^{2+} events are unique in their variability and duration and are thus better

473 qualified using the ROI-based measurements number, size and mean pixel intensity integral instead of the

474 conventional measurements such as frequency, amplitude and duration of isolated events. Indeed, unlike

475 neurons, that display well-defined Ca^{2+} signals on a millisecond scale (Chua & Morrison, 2016),

476 oligodendroglia show complex Ca^{2+} events characterized by very slow and variable kinetics which make

477 their detection and isolation difficult, in particular because of their frequent convolution (Supplementary

478 Fig. 3a-c). This complexity of oligodendroglial Ca^{2+} events has previously been observed with two-photon

479 microscopy (Balia et al., 2017) and in recordings at single cell resolution (Baraban et al., 2018; Krasnow et

480 al., 2018; Battefeld et al., 2019; Marisca et al., 2020), indicating that complex Ca^{2+} dynamics are a hallmark

481 of oligodendroglia and it is therefore essential to evaluate them in an appropriate manner. Thresholding

482 techniques or event template detection methods commonly used on neuron and astrocyte Ca^{2+} imaging

483 datasets are not easily applicable to the unique and complex Ca^{2+} events observed in oligodendroglia. To

23

484 overcome this constraint, we evaluate activity levels by measuring the number and size of active ROIs as

485 well as the integral of the traces. Our measurements thus account for the activity throughout the whole

486 ROI trace or during configurable intervals without isolating Ca^{2+} activity events. In the eventuality that a

487 detailed description of Ca^{2+} events would be desirable, extra measurements may be performed either

488 manually or by other post-processing programs on the corrected active ROI traces as output by post-

489 prOccam. In our case, we manually inspected these corrected traces and could establish that the mean

490 rise time of Ca^{2+} events easily isolated by eye lasted from few seconds to minutes, independently of the

491 imaging condition (Supplementary Fig. 3). These slow kinetics are in line with the half-width duration of 9

492 s reported for myelin internodes in the neocortex (Battefeld et al., 2019), but our results also show that

493 oligodendroglial Ca^{2+} events in lesions are poorly correlated and may have long variable durations.

494 We could successfully and automatically detect oligodendroglial-related Ca^{2+}-active ROIs in wide

495 field as well as in single cell Ca^{2+} imaging frame stacks obtained in brain slices. These *ex vivo* recordings

496 revealed significant but uncorrelated spontaneous Ca^{2+} activity in oligodendroglia inside demyelinated

497 lesions, both at the population level and at the individual cell level. In particular, our two-photon Ca^{2+}

498 imaging experiments showed that Ca^{2+} signals in ROIs located in soma or processes are not correlated,

499 suggesting that they occur independently in subcellular compartments. In this configuration, our results

500 also indicate that, compared to OLs, OPCs displayed a higher Ca^{2+} activity whose significance remain to be

501 elucidated. The experimental and analytical tools described in this study will help to further explore the

502 characteristics of these signals at different states of cell maturation and at different time points of the

503 demyelination and remyelination process. Importantly, our workflow for acquiring and analyzing *in vivo*

504 oligodendroglial Ca^{2+} signals will also allow users to investigate the role of these signals in the mammalian

505 brain in real time. We were able to corroborate that the oligodendroglial Ca^{2+} activity observed *in vivo* is

506 compatible with that observed in brain slices because it was variable but significant, poorly correlated and

507 characterized by complex slow kinetics. We also showed that Ca^{2+} activity can be stable in the same mouse

508   from one week to another. This type of *in vivo* experiments opens up new perspectives for analyzing how

509   the oligodendroglial Ca^{2+} activity changes over time during myelin repair and when the mouse is

510   performing a behavioral task.

511   In conclusion, our *ex vivo* and *in vivo* results suggest that oligodendroglial Ca^{2+} signaling plays an

512   important role during the demyelination process. Therefore, the presented experimental and analytical

513   framework will aid future investigations into oligodendroglial Ca^{2+} signaling during demyelination and

514   myelin repair. As such, it might contribute to the elucidation of Ca^{2+}-related mechanisms implicated in the

515   success or failure of remyelination in demyelinating diseases such as MS.

516 **Materials and Methods**

517 **Experimental animals**

518 All experiments followed European Union and institutional guidelines for the care and use of laboratory

519 animals and were approved by both the French ethical committee for animal care of the University Paris

520 Cité (Paris, France) and the Ministry of National Education and Research (Authorization N° 13093-

521 2017081713462292). They were performed with male and female $Pdgfra^{CreERT(+/-)};Gcamp6f^{Lox/Lox}$ or

522 $Pdgfra^{CreERT(+/-)};Gcamp5-tdTomato^{Lox/Lox}$ transgenic adult mice (7 to 9 weeks old) obtained by crossing

523 $Pdgfra^{CreERT}$ (stock 018280, The Jackson Laboratory) with $Ai95(Rcl-Gcamp6f)-D$ (stock 028865, The Jackson

524 Laboratory, USA) or $Gcamp5-tdTomato^{Lox/Lox}$ (stock 028865, The Jackson Laboratory, USA). Animals were

525 genotyped by PCR using specific primers for Cre. These mice express GCaMP6f or GCaMP5 in OPCs and

526 their progeny upon tamoxifen injection. Tamoxifen (1 mg in miglyol oil, Caesar & Loretz, Germany) was

527 administered intraperitoneally once a day for three consecutive days starting seven days before inducing

528 demyelination by LPC injection or during week 4 of CPZ administration (Fig. 1a-c). All animals had *ad*

529 *libitum* access to food and water and were exposed to a 12 hr light/dark cycle, a controlled average

530 temperature of 21 °C and 45% humidity.

531

532 **Intracranial injections of LPC to induce demyelinated lesions**

533 Mice were deeply anaesthetized using ketamine/xylazine (100/5 mg/kg, i.p.) or isoflurane (1.5 %) and

534 headfixed in a stereotaxic frame (Kopf Instruments, USA). Before starting the surgery, mice received a

535 subcutaneous injection of buprenorphine (0.1 mg/kg) as analgesic. Throughout surgical procedures mice

536 were placed on a 37 °C heating blanket and ophthalmic dexpanthenol gel (Chauvin Bausch & Lomb GmbH,

537 France) was applied to the eyes to prevent dehydration. The skin on the head was treated with betadine

538 and lidocaine and opened to expose the skull. The head was aligned using both lambda and bregma, and

539 two 0.50 mm diameter holes were bilaterally drilled in the skull at coordinates +1.40 mm anterior from

540   bregma and +0.95 and –0.95 mm lateral from the midline. The dura was removed and a glass pipette

541   connected to a Hamilton syringe containing LPC (1% in PBS; Merck, Germany) was lowered into the brain

542   until 1.80 mm depth from the brain surface reaching into corpus callosum. The pipette rested in the brain

543   for four minutes and subsequently 0.8 µL of LPC was injected two times with 4 minutes between

544   injections. After another 4 minutes the pipette was slowly retracted from the brain and the LPC injection

545   procedure was repeated in the other hemisphere. Skin was sutured (Mersilene®, EH7147H; Ethicon, USA)

546   and cleaned with betadine and mice were allowed to recover at 37 °C before returning to their home

547   cage.

548

549   **Acute brain slice preparation**

550   Acute coronal slices of 300 µm containing demyelinated lesions were prepared as previously described

551   (Mozafari et al., 2020). Brain slices were cut using a vibratome (Microm HM 650V, Thermo Scientific, USA)

552   in a chilled cutting solution containing (in mM): 93 NMDG, 2.5 KCl, 1.2 NaH2PO4, 30 NaHCO3, 20 HEPES,

553   25 Glucose, 2 urea, 5 Na-ascorbate, 3 Na-pyruvate, 0.5 CaCl2, 10 MgCl2 (pH to 7.3-7.4; 95% O2, 5% CO2)

554   and kept in cutting solution for 6 to 8 min at 34°C. Slices were transferred to a standard extracellular

555   solution at 34°C for about 20 min. Extracellular solution contained (in mM): 126 NaCl, 2.5 KCl, 1.25

556   NaH2PO4, 26 NaHCO3, 20 Glucose, 5 Na-pyruvate, 2 CaCl2, 1 MgCl2 (pH to 7.3-7.4; 95% O2, 5% CO2).

557

558   *Ex vivo* **wide-field calcium imaging**

559   Demyelinated lesions were recognized under the microscope at 4x as a brighter area in corpus callosum

560   as described previously (Sahel et al., 2015). After identifying the demyelinated lesion at 4x, cells expressing

561   GCaMP6f in the lesion were visualized with a 40x water immersion objective in a wide-field microscope

562   (Olympus BX51) using a LED system (CoolLED PE-2; Scientifica, UK) and a CCD camera (ImageQ, Optimos;

563   Scientifica, UK). Excitation and emission wavelengths were 470 nm and 525 nm, respectively. The CCD

27

564   camera and the LED system were controlled using a Digidata 1440A interface and Pclamp10.5 software

565   (Molecular Devices, USA). The image stacks were acquired at a frame rate of 1.75 Hz with 50 ms light

566   exposure for a total duration of 240 s using Micro-manager-1.4 plugin under Fiji (version 1.53k or later)

567   (Schindelin et al., 2012). Ca^{2+} imaging during bath applications of 50 µM carbachol were performed after

568   incubating the slices for five minutes with an antagonist cocktail containing 10 µM NBQX, 50 µM AP5, 10

569   µM GABAzine, 1 µM TTX and 50 µM mecamylamine.

570

571   ***Ex vivo* two-photon calcium imaging**

572   Two-Photon Ca^{2+} imaging was performed using a two-photon laser scanning microscope (Otsu et al.,

573   2014). A 40x water-immersion objective (Olympus40x LumPlanFL N 540x/0.8) in combination with a 900

574   nm excitation beam from a femtosecond Ti:Sapphire laser (10 W pump; Mira 900 Coherent, Santa Clara,

575   CA) was used to image GCaMP5 in individual putative OPCs and OLs identified by their morphology. Cells

576   with round soma and numerous processes extending towards various directions were designated OPCs,

577   while cells with elongated soma's containing thicker and more T-shaped processes were designated OLs.

578   GCaMP5 was detected with Hamamatsu photon counting PMTs through an emission filter (HQ500/40,

579   Chroma). Ca^{2+} signals of individual cells were imaged in high resolution at 3.60-6.27 frames per second

580   during 99 seconds.

581

582   **Cuprizone treatment and *in vivo* microendoscopy calcium imaging**

583   One week before starting the CPZ treatment, mice (P35-P42) were subjected to GRIN lens implantation

584   surgery (Fig. 1c). Animals were prepared for craniotomy in a stereotaxic apparatus as described above,

585   and a 1 mm diameter circular cranial window was drilled around a midpoint at coordinates +1.40 mm

586   anterior from bregma and +0.95 mm lateral from the midline. Using a blunt 23 G needle attached to a

587   vacuum pump, the cortex was aspirated in the middle of the cranial window from the top of the brain

588   surface until 1.40 mm depth. A 1.0 mm diameter GRIN lens (Inscopix, USA) was then implanted at 1.60

589   mm depth, just above the corpus callosum at the motor cortex level. This placement allows imaging inside

590   this white matter region at 1.80 mm depth as the working distance of the GRIN lenses used is ± 200 μm.

591   The lens was held in place by super glue and dental cement (Unifast, Japan) and covered with kwik-sil

592   sealant (World Precision Instruments, USA) until the baseplate surgery. Animals were allowed to recover

593   at 37°C before being transferred to their home cage.

594   For the seven days following the lens implantation procedure, animals were fed cherry or bacon

595   flavored nutragel food (Bio-Serv, France). Subsequently, we supplemented the nutragel food with 0.3%

596   CPZ (Sigma) for the 6 following weeks to induce demyelination. During week 4 of the CPZ diet, 4 daily 1

597   mg tamoxifen injections were performed intraperitoneally to induce GCaMP6f expression in

598   demyelinated areas of $Pdgfr\alpha^{CreERT(+/-)};Gcamp6f^{Lox/Lox}$ mice. During week 5 of the CPZ diet, animals were

599   subjected to a baseplating surgical procedure (Fig. 1c). Animals were anaesthesized with

600   ketamine/xylazine (100/5 mg/kg, i.p.) and the kwik-sil seal was removed from the lens. Animals were then

601   headfixed in a stereotaxic apparatus, and a miniscope V4 (Open Ephys, Portugal) with a baseplate

602   connected to it was held over the lens until a clear image of the brain surface under the lens was obtained.

603   We then cemented the baseplate onto the head of the mouse. A Ca^{2+} imaging stack was obtained during

604   the baseplating procedure to ensure that the miniscope could efficiently detect Ca^{2+} signals from the

605   demyelinated corpus callosum. Mice were recovered at 37°C and returned to their homecage. As a proof

606   of concept, $in\ vivo$ Ca^{2+} imaging was performed from week 5 of CPZ-induced demyelination (Fig. 1c). Image

607   stacks were obtained in freely moving mice with a sampling rate of 10 frames per second during 7 minutes.

608

609   **Occam and post-prOccam: an automated analytical workflow for oligodendroglial Ca^{2+} imaging data**

610   The analytical processing consists of two parts performed by two distinct software pieces thoroughly

611   described in the software user manual provided as supplementary information (Supplementary Manual).

612   Briefly, the analysis is composed of two main steps: first, the image stack is processed by Occam, a

613   Fiji/ImageJ2-based plugin written in Java (Fiji/Imagej2 version 1.53k or later); second, the data output by

614   Occam is processed by post-prOccam, a software written in Python, to both refine it and perform a series

615   of calculations on the refined data. Importantly, *ex vivo* one-photon, *ex vivo* two-photon and *in vivo*

616   microendoscopic Ca^{2+} imaging stacks are processed in slightly different ways to optimize the analysis of

617   Ca^{2+} signals acquired in these different preparations (Fig. 2a; Supplementary Manual). The softwares

618   described in this report are cross-platform Free and Open Source Software (FOSS) and licensed under the

619   GNU GPLv3+ license (available at: *https://gitlab.com/d5674/occam*).

620

621   *Preprocessing: noise correction and ROI definition.* The input for Occam is an oligodendroglial Ca^{2+} imaging

622   stack as recorded by the microscopy acquisition software. The Occam software initially performs noise

623   correction steps according to the imaging condition, and then proceeds to an automatic ROI designation

624   (Supplementary Manual). ROI designation is carried out using the machine learning-based WEKA

625   Fiji/ImageJ2 plugin that performs a trainable segmentation of frames (Arganda-Carreras et al., 2017)

626   combined with a local maxima segmentation tool. A ROI as designated by Occam is defined as a vector

627   containing the mean fluorescence intensity value of the corresponding region in the different frames of

628   the stack (that is, over the acquisition time points). Such ROI vectors are indifferently called ROI traces in

629   this report. ROIs are sorted in two different classes: 1) high and medium mean pixel intensity ROIs, that

630   correspond to Ca^{2+} active regions of the stack and 2) low mean pixel intensity ROIs, that are considered as

631   background. In this report, WEKA classifiers were trained on Ca^{2+} imaging stacks obtained from GCaMP-

632   expressing oligodendroglia in demyelinated lesions of the mouse corpus callosum in one-photon, two-

633   photon and in vivo imaging conditions, separately. Notably, training WEKA is straightforward using any

634   given set of image stacks. Occam's user interface allows one to configure various aspects of the

635   processing. For each processed image stack, Occam produces a set of comma-separated value (CSV) files

30

636   that contain the description of the mean fluorescence intensity of each ROI along the time-resolved

637   acquisition experiment. These files are then fed to the post-prOccam software.

638

639   *Post-processing: automated ROI refinement and quantifications.* The post-prOccam software is a

640   configurable software that processes the files produced by Occam. Before performing a baseline

641   subtraction, false positive ROI traces of a stack are rejected by using a sliding window-based subtraction

642   of intensities in each ROI trace and applying a detection threshold defined by the mean absolute deviation

643   (MAD) value on each subtracted trace (Supplementary Manual). Only ROIs that show significant Ca^{2+}-

644   fluorescence fluctuations are accepted for further analyses. A number of parameters configuring the ROI

645   processing and the filtering stringency can be set in a configuration file (Supplementary Files 1-3). The

646   accepted ROIs of a stack are output to a file and calculations that are then computed on these ROIs are

647   output to another file (such as the surface area of each ROI in pixels, the ROI integral, the sum integral of

648   all ROIs, the total ROI surface area in pixels, the sum integral corrected by the surface area of all ROIs, the

649   Pearson correlation between each ROI and every other ROI; Supplementary Manual). Of note, this analysis

650   can be performed on specific acquisition time point intervals of ROI traces by listing desired intervals in

651   the configuration file. The post-prOccam software logs all the processing steps and their outcome to a file

652   so as to let the user scrutinize the inner workings of the program.

653

654   **Statistical analysis**

655   Data are expressed as mean ± SEM. GraphPad Prism (version 9.3.0; GraphPad Software Inc., USA) was

656   used for statistical analysis. Each group of data was first subjected to Shapiro-Wilk normality test.

657   According to the data structure, two-group comparisons were performed using the two-tailed unpaired

658   Student's t-test or the non-parametric two-tailed unpaired Mann-Whitney U test for independent

31

659   samples; the two-tailed paired Student's t-test was used for paired samples. Multiple comparisons were

660   done with a two-way ANOVA test followed by a Bonferroni's multiple comparison test.

661

662   **Data availability**

663   The data generated and analyzed during this study are included in the manuscript and supplementary

664   files. Occam and post-prOccam programs as well as all the software documentation and a full example of

665   ex vivo widefield imaging data are hosted at *https://gitlab.com/d5674/occam* and published under a Free

666   Software GNU GPLv3+ license.

680

681   **Competing interests:** The authors have declared that no competing interests exist.

682

683   **Author contributions**

684   D.A.M. and B. M-S. conducted one-photon Ca^{2+} imaging experiments. C.H. performed two-photon Ca^{2+}

685   imaging experiments and D.A.M. performed *in vivo* microendoscopy Ca^{2+} imaging experiments. D.A.M., B.

686   M-S., C.H. and M.C.A. designed experiments and analysis. P.B., D.A.M., B. M-S wrote the ImageJ plugin.

687   M.C.A. and F.R. designed the Python software and F.R. wrote the code. D.A.M. and M.C.A. performed data

688   analyses and D.A.M., F.R. and M.C.A. wrote the manuscript. M.C.A supervised the project.

689   **References**

690   Abiraman, K., Pol, S. U., O'Bara, M. A., Chen, G.-D., Khaku, Z. M., Wang, J., Thorn, D., Vedia, B. H.,

691   Ekwegbalu, E. C., Li, J.-X., Salvi, R. J., & Sim, F. J. (2015). Anti-muscarinic adjunct therapy

692   accelerates functional human oligodendrocyte repair. *The Journal of Neuroscience: The Official*

693   *Journal of the Society for Neuroscience*, *35*(8), 3676–3688.

694   https://doi.org/10.1523/JNEUROSCI.3510-14.2015

695   Agarwal, A., Wu, P.-H., Hughes, E. G., Fukaya, M., Tischfield, M. A., Langseth, A. J., Wirtz, D., & Bergles,

696   D. E. (2017). Transient Opening of the Mitochondrial Permeability Transition Pore Induces

697   Microdomain Calcium Transients in Astrocyte Processes. *Neuron*, *93*(3), 587-605.e7.

698   https://doi.org/10.1016/j.neuron.2016.12.034

699   Bakiri, Y., Káradóttir, R., Cossell, L., Attwell, D. (2011). Morphological and electrical properties of

700   oligodendrocytes in the white matter of the corpus callosum and cerebellum. *J Physiol.* 1;589(Pt

701   3):559-73. https://doi.org/10.1113/jphysiol.2010.201376.

702   Balia, M., Benamer, N., Angulo, M.C. (2017). A specific GABAergic synapse onto oligodendrocyte

703   precursors does not regulate cortical oligodendrogenesis. *Glia,* 65(11):1821-1832.

704   https://doi.org/10.1002/glia.23197.

705   Baraban, M., Koudelka, S., & Lyons, D. A. (2018). Ca (2+) activity signatures of myelin sheath formation

706   and growth *in vivo*. *Nature Neuroscience*, *21*(1), 19–23. PubMed.

707   https://doi.org/10.1038/s41593-017-0040-x

708   Battefeld, A., Popovic, M. A., de Vries, S. I., & Kole, M. H. P. (2019). High-Frequency Microdomain Ca(2+)

709   Transients and Waves during Early Myelin Internode Remodeling. *Cell Reports*, *26*(1), 182-

710   191.e5. PubMed. https://doi.org/10.1016/j.celrep.2018.12.039

711   Cai, D.J., Aharoni, D., Shuman, T., Shobe, J., Biane, J., Song, W., Wei, B., Veshkini, M., La-Vu, M., Lou, J.,

712   Flores, S.E., Kim, I., Sano, Y., Zhou, M., Baumgaertel, K., Lavi, A., Kamata, M., Tuszynski, M.,

713   Mayford, M., Golshani, P., Silva, A.J. (2016). A shared neural ensemble links distinct contextual

714   memories encoded close in time. *Nature,* 2;534(7605):115-8.

715   https://doi.org/10.1038/nature17955.

716 Cantu, D. A., Wang, B., Gongwer, M. W., He, C. X., Goel, A., Suresh, A., Kourdougli, N., Arroyo, E. D.,

717   Zeiger, W., & Portera-Cailliau, C. (2020). EZcalcium: Open-Source Toolbox for Analysis of Calcium

718   Imaging Data. *Frontiers in Neural Circuits*, *14*, 25. https://doi.org/10.3389/fncir.2020.00025

719 Cayre, M., Falque, M., Mercier, O., Magalon, K., Durbec, P. (2021). Myelin Repair: From Animal Models

720   to Humans. *Front Cell Neurosci,* 14;15:604865. https://doi.org/10.3389/fncel.2021.604865.

721 Chittajallu, R., Aguirre, A., Gallo, V. (2004). NG2-positive cells in the mouse white and grey matter

722   display distinct physiological properties. *J Physiol.* 15;561(Pt 1):109-22.

723   https://doi.org/10.1113/jphysiol.2004.074252.

724 Chua, Y., & Morrison, A. (2016). Effects of Calcium Spikes in the Layer 5 Pyramidal Neuron on

725   Coincidence Detection and Activity Propagation. *Frontiers in Computational Neuroscience*, *10*.

726   https://doi.org/10.3389/fncom.2016.00076

727 Cohen, R. I., & Almazan, G. (1994). Rat oligodendrocytes express muscarinic receptors coupled to

728   phosphoinositide hydrolysis and adenylyl cyclase. *The European Journal of Neuroscience*, *6*(7),

729   1213–1224. https://doi.org/10.1111/j.1460-9568.1994.tb00620.x

730 De Angelis, F., Bernardo, A., Magnaghi, V., Minghetti, L., & Tata, A. M. (2012). Muscarinic receptor

731   subtypes as potential targets to modulate oligodendrocyte progenitor survival, proliferation,

732   and differentiation. *Developmental Neurobiology*, *72*(5), 713–728.

733   https://doi.org/10.1002/dneu.20976

734 Deshmukh, V. A., Tardif, V., Lyssiotis, C. A., Green, C. C., Kerman, B., Kim, H. J., Padmanabhan, K.,

735   Swoboda, J. G., Ahmad, I., Kondo, T., Gage, F. H., Theofilopoulos, A. N., Lawson, B. R., Schultz, P.

736   G., & Lairson, L. L. (2013). A regenerative approach to the treatment of multiple sclerosis.

737   *Nature*, *502*(7471), 327–332. https://doi.org/10.1038/nature12647

738   Duncan, I. D., & Radcliff, A. B. (2016). Inherited and acquired disorders of myelin: The underlying myelin

739   pathology. *Experimental Neurology*, *283*(Pt B), 452–475.

740   https://doi.org/10.1016/j.expneurol.2016.04.002

741   Franklin, R. J. M., & Ffrench-Constant, C. (2017). Regenerating CNS myelin—From mechanisms to

742   experimental medicines. *Nature Reviews. Neuroscience*, *18*(12), 753–769.

743   https://doi.org/10.1038/nrn.2017.136

744   Giovannucci, A., Friedrich, J., Gunn, P., Kalfon, J., Brown, B. L., Koay, S. A., Taxidis, J., Najafi, F., Gauthier,

745   J. L., Zhou, P., Khakh, B. S., Tank, D. W., Chklovskii, D. B., & Pnevmatikakis, E. A. (2019). CaImAn

746   an open source tool for scalable calcium imaging data analysis. *ELife*, *8*, e38173.

747   https://doi.org/10.7554/eLife.38173

748   Green, A. J., Gelfand, J. M., Cree, B. A., Bevan, C., Boscardin, W. J., Mei, F., Inman, J., Arnow, S.,

749   Devereux, M., Abounasr, A., Nobuta, H., Zhu, A., Friessen, M., Gerona, R., von Büdingen, H. C.,

750   Henry, R. G., Hauser, S. L., & Chan, J. R. (2017). Clemastine fumarate as a remyelinating therapy

751   for multiple sclerosis (ReBUILD): A randomised, controlled, double-blind, crossover trial. *Lancet*

752   *(London, England)*, *390*(10111), 2481–2489. https://doi.org/10.1016/S0140-6736(17)32346-2

753   Ingiosi, A.M., Hayworth, C.R., Harvey, D.O., Singletary, K.G., Rempe, M.J., Wisor, J.P., Frank, M.G. (2020).

754   A Role for Astroglial Calcium in Mammalian Sleep and Sleep Regulation. *Curr Biol,*

755   16;30(22):4373-4383.e7. https://doi.org/10.1016/j.cub.2020.08.052.

756   Kirischuk, S., Scherer, J., Möller, T., Verkhratsky, A., & Kettenmann, H. (1995). Subcellular heterogeneity

757   of voltage-gated Ca2+ channels in cells of the oligodendrocyte lineage. *Glia*, *13*(1), 1–12.

758   https://doi.org/10.1002/glia.440130102

759   Koizumi, S. (2010). Synchronization of Ca2+ oscillations: involvement of ATP release in astrocytes. *FEBS J,*

760   277(2):286-92. https://doi.org/10.1111/j.1742-4658.2009.07438.x.

761   Krasnow, A. M., Ford, M. C., Valdivia, L. E., Wilson, S. W., & Attwell, D. (2018). Regulation of developing

762   myelin sheath elongation by oligodendrocyte calcium transients *in vivo*. *Nature Neuroscience*,

763   *21*(1), 24–28. PubMed. https://doi.org/10.1038/s41593-017-0031-y

764   Li, J., Miramontes, T., Czopka, T., Monk, K. (2022). Synapses in oligodendrocyte precursor cells are

765   dynamic and contribute to Ca2+ activity. *bioRxiv* 2022.03.18.484955.

766   https://doi.org/10.1101/2022.03.18.484955

767   Maas, D.A., Angulo, M.C. (2021). Can Enhancing Neuronal Activity Improve Myelin Repair in Multiple

768   Sclerosis? *Front Cell Neurosci,* 15:645240. https://doi.org/10.3389/fncel.2021.645240.

769   Marisca, R., Hoche, T., Agirre, E., Hoodless, L. J., Barkey, W., Auer, F., Castelo-Branco, G., & Czopka, T.

770   (2020). Functionally distinct subgroups of oligodendrocyte precursor cells integrate neural

771   activity and execute myelin formation. *Nature Neuroscience*, *23*(3), 363–374.

772   https://doi.org/10.1038/s41593-019-0581-2

773   Moyon, S., Dubessy, A.L., Aigrot, M.S., Trotter, M., Huang, J.K., Dauphinot, L., Potier, M.C., Kerninon, C.,

774   Melik, Parsadaniantz, S., Franklin, R.J., Lubetzki, C. (2015). Demyelination causes adult CNS

775   progenitors to revert to an immature state and express immune cues that support their

776   migration. *J Neurosci,* 7;35(1):4-20. https://doi.org/10.1523/JNEUROSCI.0849-14.2015.

777   Nualart-Marti, A., Solsona, C., & Fields, R. D. (2013). Gap junction communication in myelinating glia.

778   *Biochimica Et Biophysica Acta*, *1828*(1), 69–78. https://doi.org/10.1016/j.bbamem.2012.01.024

779   Paez, P. M., & Lyons, D. A. (2020). Calcium Signaling in the Oligodendrocyte Lineage: Regulators and

780   Consequences. *Annual Review of Neuroscience*, *43*, 163–186. https://doi.org/10.1146/annurev-

781   neuro-100719-093305

782   Parys, B., Côté, A., Gallo, V., De Koninck, P., & Sík, A. (2010). Intercellular calcium signaling between

783   astrocytes and oligodendrocytes via gap junctions in culture. *Neuroscience*, *167*(4), 1032–1043.

784   https://doi.org/10.1016/j.neuroscience.2010.03.004

785   Pitman, K. A., & Young, K. M. (2016). Activity-dependent calcium signalling in oligodendrocyte

786   generation. *The International Journal of Biochemistry & Cell Biology*, *77*(Pt A), 30–34. PubMed.

787   https://doi.org/10.1016/j.biocel.2016.05.018

788   Rash, J. E., Yasumura, T., Dudek, F. E., & Nagy, J. I. (2001). Cell-specific expression of connexins and

789   evidence of restricted gap junctional coupling between glial cells and between neurons. *The*

790   *Journal of Neuroscience: The Official Journal of the Society for Neuroscience*, *21*(6), 1983–2000.

791   Remaud, S., Ortiz, F.C., Perret-Jeanneret, M., Aigrot, M.S., Gothié, J.D., Fekete, C., Kvárta-Papp, Z.,

792   Gereben, B., Langui, D., Lubetzki, C., Angulo MC, Zalc B, Demeneix B. (2017). Transient

793   hypothyroidism favors oligodendrocyte generation providing functional remyelination in the

794   adult mouse brain. *Elife,* 6:e29996. https://doi.org/10.7554/eLife.29996.

795   Sahel, A., Ortiz, F. C., Kerninon, C., Maldonado, P. P., Angulo, M. C., & Nait-Oumesmar, B. (2015).

796   Alteration of synaptic connectivity of oligodendrocyte precursor cells following demyelination.

797   *Frontiers in Cellular Neuroscience*, *9*, 77–77. https://doi.org/10.3389/fncel.2015.00077

798   Schindelin, J., Arganda-Carreras, I., Frise, E., Kaynig, V., Longair, M., Pietzsch, T., Preibisch, S., Rueden, C.,

799   Saalfeld, S., Schmid, B., Tinevez, J.-Y., White, D. J., Hartenstein, V., Eliceiri, K., Tomancak, P., &

800   Cardona, A. (2012). Fiji: An open-source platform for biological-image analysis. *Nature Methods*,

801   *9*(7), 676–682. https://doi.org/10.1038/nmeth.2019

802   Shuman, T., Aharoni, D., Cai, D.J., Lee, C.R., Chavlis, S., Page-Harley, L., Vetere, L.M., Feng, Y., Yang, C.Y.,

803   Mollinedo-Gajate, I., Chen, L., Pennington, Z.T., Taxidis, J., Flores, S.E., Cheng, K., Javaherian, M.,

804   Kaba, C.C., Rao, N., La-Vu, M., Pandi, I., Shtrahman, M., Bakhurin, K.I., Masmanidis, S.C., Khakh,

805   B.S., Poirazi, P., Silva, A.J., Golshani, P. (2020). Breakdown of spatial coding and interneuron

806   synchronization in epileptic mice. *Nat Neurosci*, 23(2):229-238. https://doi.org/10.1038/s41593-

807   019-0559-0.

808 Takeda, M., Nelson, D. J., & Soliven, B. (1995). Calcium signaling in cultured rat oligodendrocytes. *Glia*,

809   *14*(3), 225–236. https://doi.org/10.1002/glia.440140308

810 Venugopal, S., Srinivasan, R., & Khakh, B. S. (2019). GECIquant: Semi-automated Detection and

811   Quantification of Astrocyte Intracellular Ca2+ Signals Monitored with GCaMP6f. In M. De Pittà &

812   H. Berry (Eds.), *Computational Glioscience* (pp. 455–470). Springer International Publishing.

813   https://doi.org/10.1007/978-3-030-00817-8_17

814 Wang, Y., DelRosso, N. V., Vaidyanathan, T. V., Cahill, M. K., Reitman, M. E., Pittolo, S., Mi, X., Yu, G., &

815   Poskanzer, K. E. (2019). Accurate quantification of astrocyte and neurotransmitter fluorescence

816   dynamics for single-cell and population-level physiology. *Nature Neuroscience*, *22*(11), 1936–

817   1944. https://doi.org/10.1038/s41593-019-0492-2

818 Wang, Y., Shi, G., Miller, D. J., Wang, Y., Wang, C., Broussard, G., Wang, Y., Tian, L., & Yu, G. (2017).

819   Automated Functional Analysis of Astrocytes from Chronic Time-Lapse Calcium Imaging Data.

820   *Frontiers in Neuroinformatics*, *11*, 48. https://doi.org/10.3389/fninf.2017.00048

821 Welliver, R. R., Polanco, J. J., Seidman, R. A., Sinha, A. K., O'Bara, M. A., Khaku, Z. M., Santiago González,

822   D. A., Nishiyama, A., Wess, J., Feltri, M. L., Paez, P. M., & Sim, F. J. (2018). Muscarinic Receptor M

823   ₃ R Signaling Prevents Efficient Remyelination by Human and Mouse Oligodendrocyte Progenitor

824   Cells. *The Journal of Neuroscience*, *38*(31), 6921–6932.

825   https://doi.org/10.1523/JNEUROSCI.1862-17.2018

826 Xu, Y. K. T., Call, C. L., Sulam, J., & Bergles, D. E. (2021). Automated *in vivo* Tracking of Cortical

827   Oligodendrocytes. *Frontiers in Cellular Neuroscience*, *15*, 667595.

828   https://doi.org/10.3389/fncel.2021.667595

829   Yuan et al 2015 Tianyi Yuan, T., Lu, J., Zhang, J., Zhang, Y., Chen, L. (2015). Spatiotemporal detection and

830   analysis of exocytosis reveal fusion "hotspots" organized by the cytoskeleton in endocrine cells.

831   *Biophysical journal, 108(*2), 251–260. https://doi.org/10.1016/j.bpj.2014.11.3462

832   Zhang, L., Liang, B., Barbera, G., Hawes, S., Zhang, Y., Stump, K., Baum, I., Yang, Y., Li, Y., Lin, D.T. (2019).

833   Miniscope GRIN Lens System for Calcium Imaging of Neuronal Activity from Deep Brain

834   Structures in Behaving Animals. *Curr Protoc Neurosci,* 86(1):e56.

835   https://doi.org/10.1002/cpns.56.